Heterochromatin protects retinal pigment epithelium cells from oxidative damage by silencing p53 target genes

Lili Gong[a,1,2], Fangyuan Liu[a,1], Zhen Xiong[a,1], Ruili Qi[a,1], Zhongwen Luo[a,1], Xiaodong Gong[a], Qian Nie[a,b], Qian Sun[a], Yun-Fei Liu[a], Wenjie Qing[a,b], Ling Wang[a,b,c], Lan Zhang[a], Xiangcheng Tang[a], Shan Huang[a], Gen Li[a], Hong Ouyang[a], Mengqing Xiang[a,d,e], Quan Dong Nguyen[f], Yizhi Liu[a,2], and David Wan-Cheng Li[a,b,c,2]

[a]State Key Laboratory of Ophthalmology, Zhongshan Ophthalmic Center, Sun Yat-sen University, Guangzhou, 510060 Guangdong, China; [b]Key Laboratory of Protein Chemistry and Developmental Biology, College of Life Sciences, Hunan Normal University, Changsha, 410081 Hunan, China; [c]Truhlsen Eye Institute, University of Nebraska Medical Center, Omaha, NE 68198; [d]Center for Advanced Biotechnology and Medicine, Rutgers Robert Wood Johnson Medical School, Piscataway, NJ 08854; [e]Department of Pediatrics, Rutgers Robert Wood Johnson Medical School, Piscataway, NJ 08854; and [f]Byers Eye Institute, Stanford University School of Medicine, Palo Alto, CA 94303

Oxidative stress (OS)-induced retinal pigment epithelium (RPE) cell apoptosis is critically implicated in the pathogenesis of age-related macular degeneration (AMD), a leading cause of blindness in the elderly. Heterochromatin, a compact and transcriptional inert chromatin structure, has been recently shown to be dynamically regulated in response to stress stimuli. The functional mechanism of heterochromatin on OS exposure is unclear, however. Here we show that OS increases heterochromatin formation both in vivo and in vitro, which is essential for protecting RPE cells from oxidative damage. Mechanistically, OS-induced heterochromatin selectively accumulates at p53-regulated proapoptotic target promoters and inhibits their transcription. Furthermore, OS-induced desumoylation of p53 promotes p53–heterochromatin interaction and regulates p53 promoter selection, resulting in the locus-specific recruitment of heterochromatin and transcription repression. Together, our findings demonstrate a protective function of OS-induced heterochromatin formation in which p53 desumoylation-guided promoter selection and subsequent heterochromatin recruitment play a critical role. We propose that targeting heterochromatin provides a plausible therapeutic strategy for the treatment of AMD.

age-related macular degeneration | oxidative stress | RPE | heterochromatin | p53

The retinal pigment epithelium (RPE) is the pigmented cell layer of the retina that supports and nourishes photoreceptors (1). Because of the intense illumination from focal light, the high oxygen tension in the macular area, and the phagocytosis of photoreceptor outer segments, RPE cells are particularly sensitive to oxidative stress (OS). Strong evidence supports the hypothesis that cumulative OS-induced RPE apoptosis is a major factor in the etiology of age-related macular degeneration (AMD), the primary cause of blindness in elderly persons (2, 3). Although OS-induced gene regulation in RPE cells has been well studied, little is known about the functions of gene-poor heterochromatin during this process. In fact, heterochromatin, which is generally associated with the maintenance of gene silencing, is also dynamically regulated in response to stress (4).

Chromatin is divided into euchromatin and heterochromatin based on differential compaction during interphase, with heterochromatin being highly condensed, existing in transcriptional inert conformation (5). Heterochromatin is generated and maintained by epigenetic modifications, mainly trimethylation of histone 3 lysine 9 (H3K9me3), in which suppressor of variegation 3–9 homolog 1 (*Drosophila*) (SUV39H1) is the principle methyltransferase (6). Embedded within heterochromatin is a group of highly repetitive DNA sequences, known as satellite DNAs, that give rise to noncoding satellite RNAs (7). Satellite DNA is

thought to be maintained in a transcriptionally silenced state by the repressive H3K9me3 mark; however, aberrant satellite transcription can cause heterochromatin disorganization and genome instability, which have been linked to carcinogenesis (8, 9). We and others have recently found that repression of satellite is a critical mechanism by which tumor suppressors protect genome stability (8, 10).

The H3K9me3 mark has been detected on p53-regulated gene promoters, which can be abrogated on p53 activation by MDM2-mediated SUV39H1 degradation (11, 12). How ubiquitously distributed heterochromatin accumulates at specific p53 target loci and mediates stress response is currently unknown, however. The interaction of p53 with chromatin is tightly regulated by its posttranslational medications, among which sumoylation has been shown to prevent p53 binding to DNA in vitro (13). Nevertheless, the function of p53 sumoylation in vivo is largely undefined, as both activation and inhibition of its downstream gene transcription were observed (13–15).

Significance

Oxidative stress-induced damage to retinal pigmented epithelial (RPE) cells is critically implicated in the pathogenesis of age-related macular degeneration (AMD), a leading cause of blindness in the elderly. Here we report that oxidative stress-induced heterochromatin formation is essential to promote RPE survival. Mechanistically, oxidative damage-induced formation of heterochromatin occurs at the 53 target promoters of apoptosis genes and is regulated by p53 sumoylation. Our study demonstrates mechanistic links among chromatin conformation, p53 sumoylation, and RPE cell death. We propose that targeting heterochromatin provides a novel strategy for AMD treatment.

CELL BIOLOGY

In the present study, we used mouse models and cultured human RPE cells to investigate the functional mechanism of heterochromatin on OS exposure. We found that OS-induced heterochromatin formation occurs both in vitro and in vivo. Pharmaceutical and genetic approaches demonstrated that the formation of heterochromatin was essential for the survival of OS-exposed RPE cells. Mechanistically, the OS-induced H3K9me3 heterochromatin on p53 target promoters silenced the transcription of p53-dependent apoptotic genes, which was regulated by the desumoylation of p53. Together, our results present a mechanism regulating the interaction between p53 and heterochromatin during OS exposure, which has a previously unknown protective function.

Results

OS Increases Heterochromatin Formation in RPE Cells. To ascertain RPE heterochromatin status on OS exposure, mice were injected with sodium iodate (NaIO$_3$), a stable oxidizing agent that targets primarily the RPE (16). Consistent with previous reports, NaIO$_3$ injection led to significant thinning of the retina and disruption of the RPE structure (Fig. 1 *A* and *B*). Interestingly, we observed dramatically increased H3K9me3 immunofluorescence (IF) signals in RPE cells on OS exposure (Fig. 1 *B*, *a*). The number of H3K9me3-positive RPE cells was increased by approximately seven-fold in NaIO$_3$-injected mice compared with mice receiving mock treatment (Fig. 1 *B*, *c*). In addition, the average number of distinct heterochromatin foci per cell, as labeled by H3K9me3, was increased from 2.73 to 4.81 (Fig. 1 *B*, *b* and *d*). Western blot (WB) analysis further showed that H3K9me3 was profoundly up-regulated in NaIO$_3$-injected retinas compared with mock-treated retinas (Fig. 1*C*).

To determine the functional importance of the observed heterochromatin induction, we investigated the transcriptional status of known heterochromatic loci in RPE cells. Quantitative RT-PCR (qRT-PCR) showed significantly reduced expression of murine satellite RNAs (major satellite) on OS exposure (Fig. 1*D*). We next sought to determine the heterochromatin status in human cells using the well-established RPE cell line ARPE-19 and primary human RPE (hRPE) cells. Because H$_2$O$_2$ delivered as single pulse is rapidly depleted in cultured cells, we used 10 mU/mL glucose oxidase (GO), which continuously generates cytotoxic H$_2$O$_2$ levels (65–150 μM in a 24-h period) to treat RPE cells (17) (Fig. S1 *A–C*). We then performed a micrococcal nuclease (MNase) sensitivity assay in ARPE-19 cells. MNase cleaves preferentially at linker DNA lying between individual nucleosomes; thus, the sensitivity of the genomic DNA to MNase reflects chromatin condensation (18). Markedly increased chromatin compaction was found on OS exposure (Fig. 1*E*). These results suggest that more heterochromatin was formed in human RPE cells after OS exposure; indeed, significant up-regulation of the H3K9me3 signal was detected compared with control cells (Fig. 1*F* and Fig. S1*D*).

Heterochromatin formation silences satellite transcription. We conducted quantitative chromatin immunoprecipitation (qChIP) experiments to determine the presence of H3K9me3 at the human satellite locus. As shown in Fig. 1*G*, OS significantly increased the H3K9me3 mark at the satellite locus but not at the short interspersed *Alu* repetitive elements. Consistent with increased H3K9me3 modification, dramatically decreased amounts of satellite transcripts were found in OS-exposed cells (Fig. 1*H*). Furthermore, transcription repression was specific to satellite, as *Alu* transcripts were up-regulated on OS exposure (Fig. S2). Finally, we found that IL-18, which is known to be involved in AMD pathogenesis (19), also increased H3K9me3 levels, whereas inclusion of antioxidant *N*-acetylcysteine prevented such up-regulation (Fig. S1*E*), suggesting that OS-induced heterochromatin formation may also exist in the inflammation response.

Together, the foregoing findings indicate that OS increased heterochromatin formation, and that the induced heterochromatin functionally silenced satellite transcription both in vitro and in vivo.

Heterochromatin Is Needed to Protect RPE from OS-Induced Apoptosis. To determine the biological functions of OS-induced heterochromatin formation, we first treated mice by oral gavage with vehicle control or chaetocin, a selective inhibitor of SUV39 methyltransferases that methylate H3K9 (20). Chaetocin alone had no obvious effect on RPE morphology; however, chaetocin treatment dramatically sensitized RPE cells to OS, leading to disruption of the RPE structure under low levels of NaIO$_3$ and marked RPE degeneration at higher dosages (Fig. 2*A*). We next assessed the effects of chaetocin on hRPE cells. Similar to the effects observed in mouse RPE, exposure to chaetocin alone did not affect hRPE cell viability, but it did increase apoptosis in OS-exposed cells (Fig. 2*B*). Overexpression of satellite transcripts is a hallmark of heterochromatin destabilization; thus, we transfected human and mouse satellite into hRPE cells, and detected increased apoptosis also in satellite-overexpressing cells on OS exposure (Fig. 2*C* and Fig. S3). Together, these results suggest that heterochromatin maintenance is required for RPE survival upon OS exposure.

We next sought to determine whether drugs known to protect RPE cells from OS affect heterochromatin formation or maintenance. Resveratrol (RSV) is a well-recognized compound that protects RPE from OS (21, 22). A 3-(4,5-dimethylthiazol-2-yl)-2,5-diphenyltetrazolium bromide tetrazolium (MTT) assay showed that RSV increased cell viability in both the absence and the presence of OS, consistent with its stimulation of mitochondrial biosynthesis (Fig. S4*A*). Notably, increasing RSV concentrations led to greater chromatin compaction, increased H3K9me3 levels, and suppressed satellite transcription (Fig. 2 *D–F*). Because RSV also exhibits strong antioxidant effects, we tested whether the protective function of RSV relayed on heterochromatin formation. To this end, we administered a combination of RSV with chaetocin in the presence of OS. IF staining for ZO-1 tight junction, RPE barrier function analysis, and flow cytometry analysis showed that RSV protection on RPE was reversed by chaetocin treatment (Fig. 2*G* and Fig. S4 *B and C*). Therefore, the ability to promote heterochromatin formation is essential for RSV to resist on OS in RPE cells.

Finally, to directly evaluate the effects of increased heterochromatin formation in cell protection, WT SUV39H1 (SUVWt) or catalytically inactivated mutant SUV39H1 (SUVH324L) (23) was transfected into hRPE cells. As expected, SUVWt increased, but SUVH324L decreased, H3K9me3 levels (Fig. 2*H*). In the presence of OS, RPE-SUVWt cells displayed ~50% decreased apoptosis, while RPE-SUVH324L showed profoundly increased apoptosis compared with vector-transfected cells (Fig. 2*I*). Together, these results further suggest that heterochromatin formation protects RPE cells from oxidative damage, and that heterochromatin destabilization promotes OS-induced RPE cell injury.

Heterochromatin Suppresses p53-Mediated Apoptosis Signaling. To define the underlying mechanism through which heterochromatin protects RPE cells from OS, we systematically investigated RPE transcriptome alterations in the presence of heterochromatin destabilization induced by satellite α overexpression. Microarray analysis identified 222 RefSeq genes that showed differential expression upon satellite α transfection (1.5-fold change; $P < 0.01$) (Fig. S5). Content analysis (Gene Ontology) showed that the altered genes were implicated in spindle organization, sister chromatid segregation, and DNA damage response, which is consistent with the reported effects of satellite overexpression on mitotic catastrophe and DNA damage (8) (Fig. S5). Interestingly, Kyoto Encyclopedia of Genes and Genomes (KEGG) pathway analysis indicated that these genes were enriched for the p53 signaling pathway ($P < 0.01$) (Fig. 3*A*).
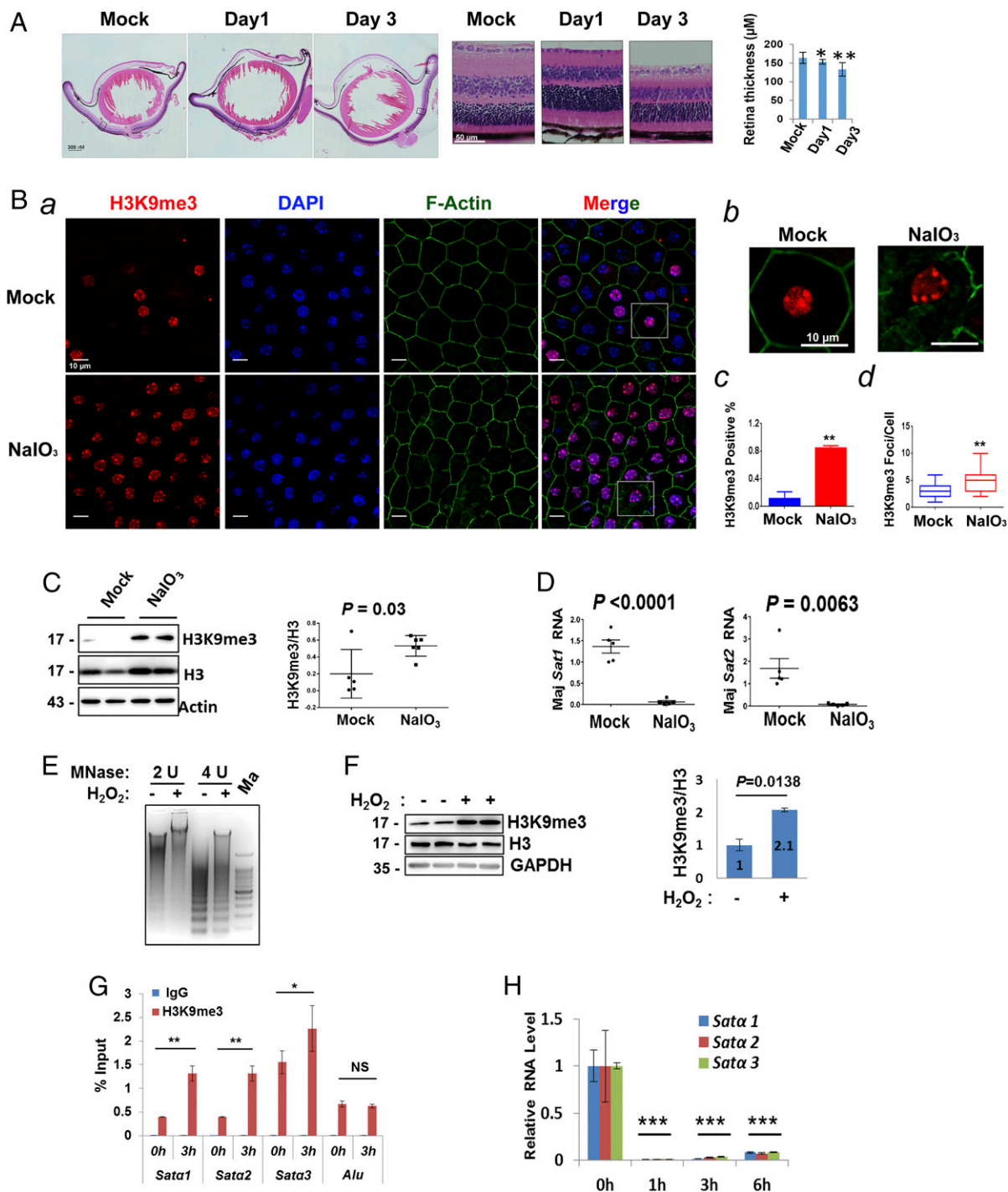
Fig. 1. OS induces heterochromatin formation. (*A*) Histological sections of mouse eye stained with hematoxylin and eosin at 1 d after 70 mg/kg NaIO₃ injection compared with PBS (mock) injection. Selected regions show significantly thinner retinal thickness in the NaIO₃-treated mice compared with the mock-treated group. $n = 3$/group. *$P < 0.05$; **$P < 0.01$. (*B*) Flat mount showing mouse RPE structure. Confocal microscopic observations were made at day 1 postinjection. (*a* and *b*) The RPE structure was demonstrated by F-actin labeled by FITC-phalloidin. Heterochromatin foci were demonstrated by H3K9me3 staining. (*c*) The H3K9me3-positive cells were manually counted and plotted ($n = 950$ cells/group). $n = 3$ mice/group. **$P < 0.0005$. (*d*) The numbers of H3K9me3-stained nuclear foci per cell ($n = 100$ cells/group) were counted and plotted. $n = 4$ mice/group. **$P < 0.0005$. (*C*) Increased H3K9me3 levels in mouse retina in response to OS exposure. (*Left*) Representative WB analysis of H3K9me3 levels in mouse retina in the presence or absence of NaIO₃ injection. (*Right*) Immunoblots from five independent experiments were quantified and plotted. (*D*) qRT-PCR analysis showing significant decreases in two mouse satellites (*Left*: Maj Sat1; *Right*: Maj Sat2) in NaIO₃-treated RPE cells compared with mock-treated cells ($n = 5$/group). Ct values of each sample were normalized with the Ct value of 18S rRNA. (*E*) ARPE-19 cells were treated for 3 h with (+) or without (−) 10 mU/mL GO. After digestion of the nuclei with micrococcal nuclease (MNase) for 5 min at the indicated units, genomic DNA was extracted and separated by a 1.2% agarose gel. Ma: 200-bp DNA marker. (*F, Left*) WB analysis showing increased H3K9me3 levels in ARPE-19 cells on OS exposure. (*F, Right*) Quantification of the blots. Values are mean ± SD. $n = 3$. (*G*) qChIP experiments showing enrichment of H3K9me3 to three human satellite α (Satα1, 2, and 3) and *Alu* regions. The relative H3K9me3 over the 2% input is shown. Error bars represent SD. $n = 3$. NS, not significant. *$P < 0.05$; **$P < 0.0005$. (*H*) qRT-PCR analysis showing satellite α expression. ***$P < 0.0001$. All P values were calculated by the unpaired *t* test.
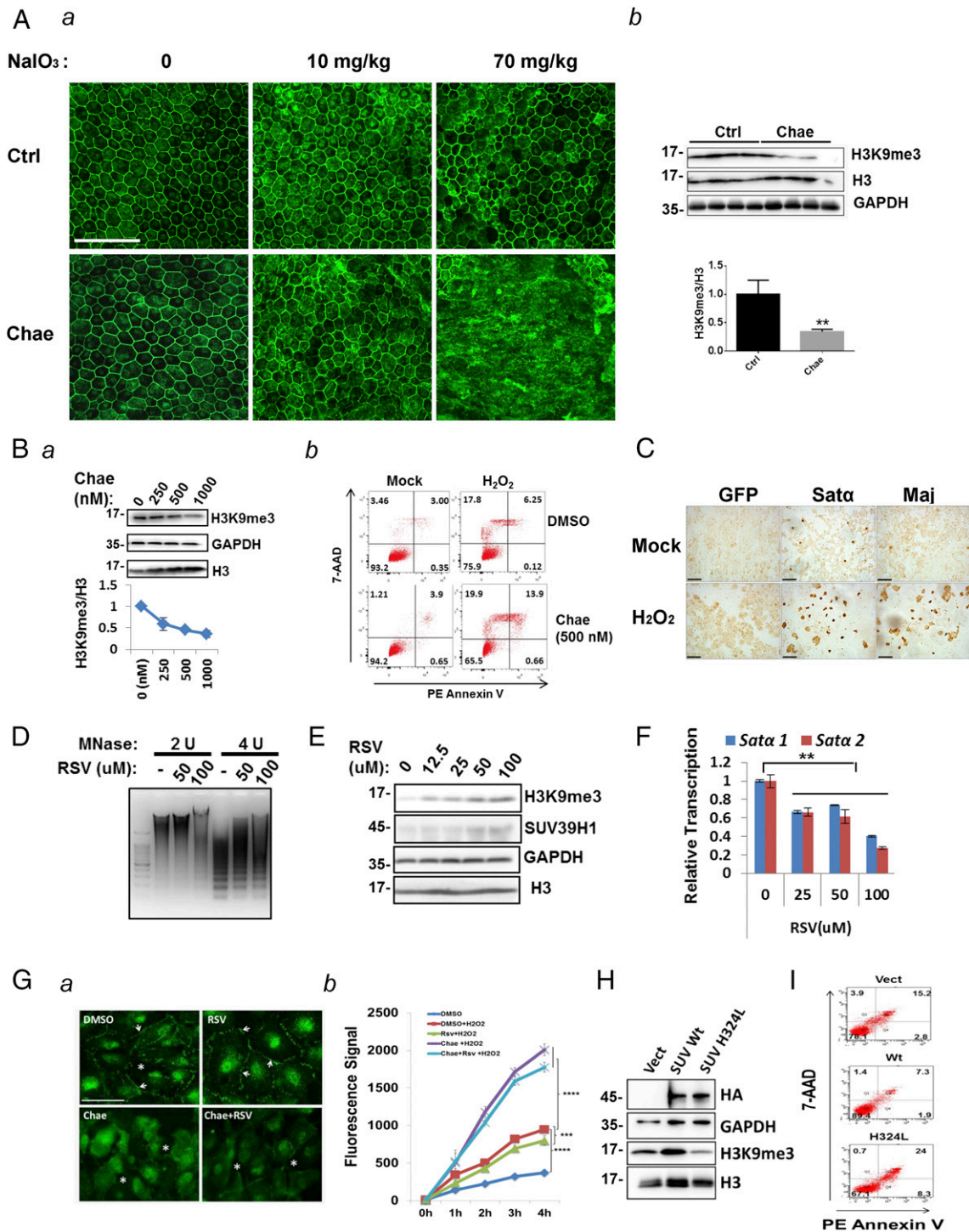
Gong et al.

www.manaraa.com

Fig. 2. Heterochromatin is needed to protect RPE cells from OS. (*A*) Chaetocin treatment sensitizes mouse RPE cells to OS. Mice were treated by oral gavage with PEG400 [control (Ctrl)] or 0.25 mg/kg chaetocin (Chae) for 6 d before injection of NaIO$_3$ or PBS. (*a*) Fluorescent microscopy of F-actin showing the RPE structure at day 1 postinjection. $n = 6$/group. (Scale bar: 100 μm.) (*b*, *Upper*) WB analysis of H3K9me3 levels in four Ctrl or Chae-treated mouse retinas and RPE cells. (*b*, *Lower*) Quantification of the immunoblots. **$P < 0.0005$. (*B*) Chaetocin treatment sensitizes human RPE cells to OS. (*a*) WB analysis of H3K9me3 level in hRPE cells with the indicated Chae treatment. Quantification is derived from two independent experiments. (*b*) Cell apoptosis determined by flow cytometry analysis. RPE cells with the indicated treatment were stained with phycoerythrin annexin V (PE) and 7-amino-actinomycin (7-AAD) before flow cytometry analysis. Numbers indicate cell percentage in each gate. (*C*) TUNEL analysis of cell apoptosis in hRPE cells expressing indicated plasmids. (Scale bar: 100 μm.) (*D*) RPE cells treated with indicated concentrations of RSV were subjected to MNase digestion, as described in Fig. 1*E*. (*E*) WB showing increased H3K9me3 and SUV39H1 levels in RPE cells with the indicated RSV treatment. (*F*) qRT-PCR analysis of two groups of satellite α transcripts. **$P < 0.01$. (*G*) Effects of heterochromatin on RPE cell tight junctions and monolayer permeability. ARPE-19 cells were treated with the indicated compounds for 24 h, followed by exposure to OS for 6 h. (*a*) ZO-1 was detected by IF study. Arrows indicate the presence of ZO-1 tight junctions, *Breakages in cell periphery. (*b*) Transepithelial permeability analyzed with 40-kDa FITC-dextran over a 4-h culture period, inward (upper to lower chamber). Values are mean ± SD. ****$P < 0.0001$; **$P < 0.005$. (*H*) WB analysis of ectopic expression of FLAG vector, FLAG-SUV39H1 WT, or H324L mutant in hRPE cells. The effects on heterochromatin were demonstrated by H3K9me3 levels. (*I*) Flow cytometry analysis of apoptosis in RPE cells transfected with the indicated plasmids and exposed to OS for 6 h.
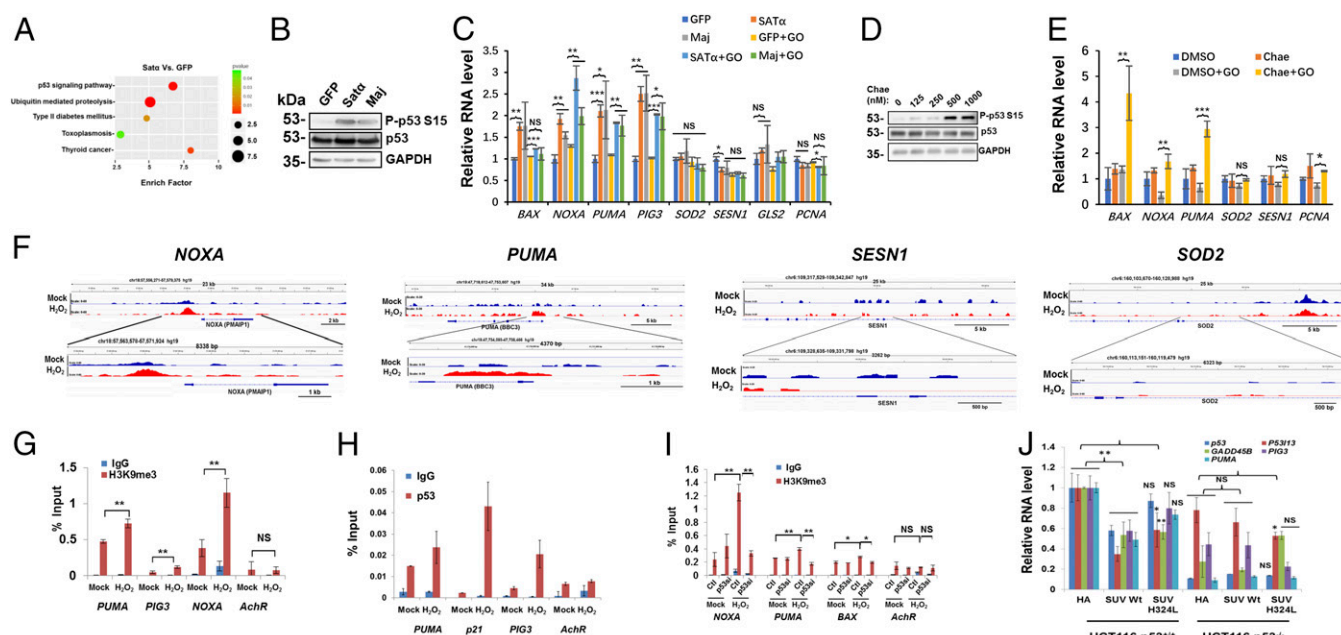
Fig. 3. Heterochromatin primarily suppresses the p53-mediated apoptosis pathway. OS was generated by treatment with 10 mU/mL GO for 3 h in the indicated assays. (*A*) KEGG enrichment analysis of genes with significant expression changes in satellite α- vs. GFP-transfected ARPE-19 cells (1.5-fold change; $P <$ 0.01). (*B*) WB analysis of p53Ser15 phosphorylation in GFP-, satellite α-, or major satellite-transfected ARPE-19. (*C*) qRT-PCR analysis of p53-regulated apoptotic genes in ARPE-19 transfected with indicated plasmids with or without OS exposure. **$P <$ 0.005; *$P <$ 0.05. (*D*) WB analysis of p53ser15 phosphorylation in ARPE-19 treated with indicated concentrations of chaetocin for 24 h. (*E*) qRT-PCR analysis of p53-regulated genes in ARPE-19 with or without 500 nM chaetocin treatment for 24 h before further OS exposure. *$P <$ 0.05; **$P <$ 0.005; ***$P <$ 0.001. (*F*) ChIP-seq analysis of H3K9me3 signals in ARPE-19. (*G* and *H*) qChIP experiments showing increased H3K9me3 and p53 occupancy on p53 target promoters on OS exposure. (*I*) qChIP experiments showing H3K9me3 occupancy on p53 target gene promoters in control (Ctrl) or p53 knockdown (p53si) hRPE cells. p53 knockdown efficiency is shown in Fig. S8. siRNA#1 was selected in ChIP experiments. Error bars represent SD ($n =$ 2). *$P <$ 0.05; **$P <$ 0.01. (*J*) qRT-PCR analysis of p53-regulated transcripts in HCT116 p53$^{+/+}$ and HCT116 p53$^{-/-}$ cells transfected with indicated plasmids. $n =$ 3. *$P <$ 0.05; **$P <$ 0.01.

p53 is a major sensor of stress stimuli, including OS, and p53 phosphorylation at Ser15 was dramatically induced on human or mouse satellite overexpression, or in response to OS exposure, suggesting p53 activation (Fig. 3*B* and Fig. S6). We further validated the microarray results and examined several p53-mediated apoptotic genes in the presence or absence of OS. qRT-PCR showed that proapoptotic genes *NOXA*, *PUMA*, and *PIG3* were significantly up-regulated in the satellite-overexpressing cells, but p53-regulated cell cycle or antioxidation genes were largely unaltered (Fig. 3*C* and Fig. S5*C*). In addition, perturbation of heterochromatin by chaetocin also led to phosphorylation of p53Ser15 and consequent induction of proapoptotic gene transcription on OS exposure (Fig. 3 *D* and *E*). Therefore, these data indicate that p53 sensed heterochromatin instability, and that heterochromatin primarily repressed p53-mediated proapoptotic genes on OS exposure.

Heterochromatin suppresses transcription through formation of the repressive H3K9me3 mark. To examine whether heterochromatin directly binds to the p53-mediated genes, we performed H3K9me3 ChIP sequencing (ChIP-seq) analysis. We found that OS increased the presence of H3K9me3 on *NOXA* and *PUMA* gene promoters, but H3K9me3 signals were absent on the p53-regulated antioxidant (*SESN1* and *SOD2*) or cell cycle (*PCNA* and *p21*) gene loci with known p53-binding sites, suggesting a gene context-dependent recruitment of heterochromatin (Fig. 3*F* and Fig. S7). ChIP-quantitative PCR (qPCR) further confirmed that OS exposure enhanced H3K9me3 binding to the promoters of *NOXA*, *PUMA*, and *PIG3* (Fig. 3*G*). Previous studies have shown that adenoviral protein-induced heterochromatin prevented p53 access to its target promoters (24). We tested whether p53 was excluded from target promoters by OS-induced heterochromatin. qChIP analysis showed that p53

was accumulated on, rather than blocked from, its target gene promoters on OS exposure (Fig. 3*H*). The simultaneously increased p53 and occupancy of H3K9me3 density led us to hypothesize that p53 might be involved in OS-induced heterochromatin formation. We tested our hypothesis by a ChIP assay in p53-silenced hRPE cells (Fig. S8). Knockdown of p53 did not affect H3K9me3 occupancy under normal conditions; however, OS-induced H3K9me3 recruitment was suppressed when p53 was depleted (Fig. 3*I*). These results suggest that p53 is required for heterochromatin-mediated gene silencing. To further confirm this, we overexpressed SUV39H1Wt and the inactive SUV39H1H324L mutant into HCT116 p53$^{+/+}$ and HCT116 p53$^{-/-}$ cells. qRT-PCR showed that SUV39H1 repressed expression of p53 target genes only in the presence of WT p53 ($P <$ 0.05) (Fig. 3*J*). Furthermore, H324L mutant had no significant repressive effects on several p53 target genes, including *p53*, *PIG3*, and *PUMA* (Fig. 3*J*). Therefore, these data demonstrate that functional heterochromatin is essential for repressing p53-dependent apoptotic gene transcription.

Desumoylation of p53 Modulates p53 Promoter Selection and Promotes Heterochromatin-Mediated Target Gene Silencing. We next sought to investigate how p53 directs heterochromatin-mediated repression of proapoptotic genes. A previous study indicated that SUV39H1 forms a complex with p53 that is capable of methylating H3K9, and that MDM2 serves as a scaffold for formation of this complex (25). We observed an interaction between p53 and SUV39H1 that was enhanced in response to OS exposure (Fig. 4*A*). However, the association between MDM2 and p53 was attenuated on OS, indicating that the enhanced p53–heterochromatin binding is unlikely derived from the MDM2-mediated scaffolding (Fig. S9). Interestingly, we
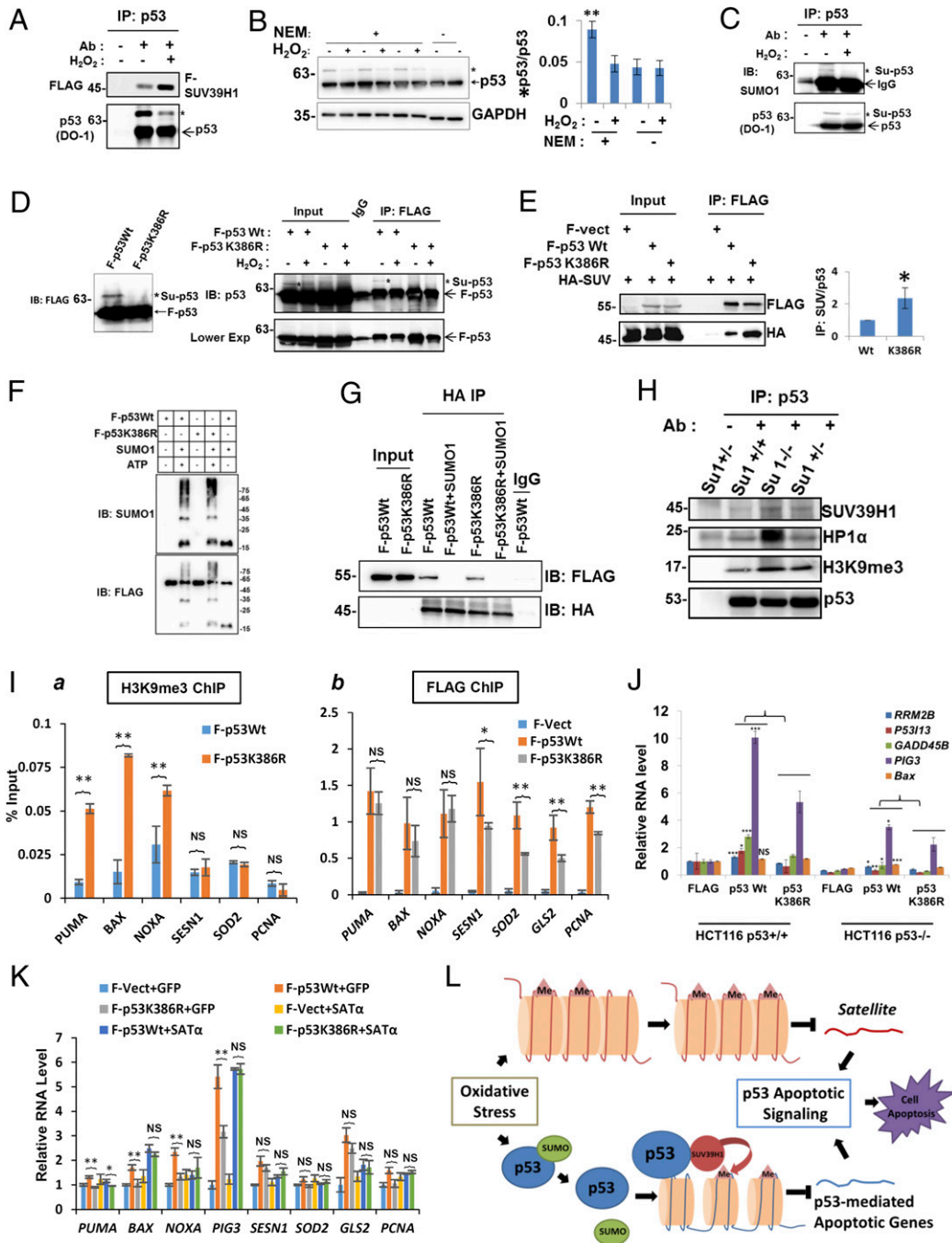
Gong et al.

CELL BIOLOGY

Fig. 4. Desumoylation of p53 is needed for heterochromatin-mediated p53 target gene repression. (*A*) FLAG-SUV39H1 was transfected into hRPE cells. The endogenous p53 protein was precipitated by p53 antibody DO-1, and a 67-kDa form of p53 was detected (labeled with *). The co-IP experiment was conducted in the presence of a desumoylation inhibitor, 20 mM NEM. (*B*) The 67-kDa p53 decreases on OS exposure. WB analysis showing the conventional p53 and a 67-kDa species. Quantification of the percentage of the 67-kDa p53 species (*p53) relative to the total p53. $n = 3$. **$P < 0.005$. (*C*) Decreased p53 modification by SUMO1 on OS exposure. Endogenous p53 protein was immunoprecipitated from hRPE cells with or without OS exposure. The precipitates were immunoblotted with the p53 (DO-1) antibody, then reprobed with antibody to SUMO1. (*D*) OS led to desumoylation of p53 at K386. (*Left*) WB analysis of FLAG-p53 WT (F-p53 WT) or FLAG-p53 K386R (F-p53 K386R). *Sumoylated p53 (Su-p53). (*Right*) IP analysis showing desumoylation of p53 on OS exposure. The FLAG immunoprecipitates were immunoblotted for p53. (*E*) Co-IP demonstrating that desumoylation of p53 increased its binding to SUV39H1. hRPE cells were transfected with indicated plasmids. WT or K386R p53 was precipitated by anti-FLAG antibody, and the associated SUV39H1 was detected by HA antibody. Quantification was done from two independent experiments. *$P < 0.05$. (*F*) In vitro sumoylation of p53 WT or K386R by SUMO1. (*G*) In vitro protein-binding assay showing that sumoylation of p53 abolished its interaction with SUV39H1. (*H*) Co-IP showing increased p53–heterochromatin interaction in SUMO1 knockout mouse retinas. Endogenous p53 was immunoprecipitated from 2-mo-old SUMO1 WT (Su1^{+/+}), knockout (Su1^{-/-}), and heterozygous (Su1^{+/-}) mouse retinas. The major heterochromatin components were detected in the precipitates by WB. (*I*) qChIP showing H3K9me3 (*a*) and p53 (*b*) occupancy on the indicated promoters in hRPE cells. Error bars represent SD. $n = 2$. *$P < 0.05$; **$P < 0.01$. (*J*) qRT-PCR analysis of p53 target genes in HCT116 p53^{+/+} or HCT116 p53^{-/-} cells transfected with indicated plasmids. (*K*) qRT-PCR analysis of gene expression in HCT116 p53^{-/-} cells transfected with indicated plasmids. (*L*) Two mechanisms were proposed for how heterochromatin prevents RPE cells from oxidative damage: (*i*) heterochromatin represses aberrant transcription of satellite to prevent activation of the p53 apoptotic pathway, or (*ii*) heterochromatin interacts with desumoylated p53, resulting in selective formation of H3K9me3 marks on p53-regulated proapoptotic target promoters and transcription repression.

repeatedly observed an ∼67-kDa protein species detected by the p53 antibody (DO-1). Furthermore, OS decreased the amount of the 67-kDa protein (labeled by *), while enhancing p53–SUV39H1 binding (Fig. 4A). Inclusion of N-ethylmaleimide (NEM), an inhibitor of desumoylases, during cell lysis, increased the detection of this p53 species, which represented ∼9% of the total p53 (Fig. 4B). Monosumoylation could explain the apparent ∼15-kDa increase in molecular mass. Indeed, in p53 immunoprecipitates, the 67-kDa isoform of p53 reacted with the antibody to SUMO1, whose signal decreased in the presence of OS (Fig. 4C). Previous studies have identified K386 of p53 as the SUMO1 modification site (14, 15). Indeed, OS led to desumoylation of the WT p53 without affecting the sumoylation-deficient p53 K386R mutant (Fig. 4D). These data suggest that p53 desumoylation is closely associated with increased interactions with heterochromatin SUV39H1.

To ascertain whether such a correlation represents a causal link, we conducted three lines of experiments. First, co-immunoprecipitation (co-IP) was performed to compare the binding of p53Wt or K386R mutant to SUV39H1. We found that K386R exhibited a more than twofold increase in binding to SUV39H1 relative to WT p53 (Fig. 4E). Next, an in vitro p53 sumoylation assay was conducted to directly address the effects of sumoylation on p53–SUV39H1 interaction. Unlike the in vivo conditions where mutation of K386 abolished p53 sumoylation (Fig. 4D), the in vitro reaction demonstrated that the K386R mutant could be sumoylated equally as well as WT p53 (Fig. 4F). We reason that such differences arise from the absence of desumoylation enzymes during the in vitro reaction, which may result in stabilization of sumoylation on noncanonical lysine residues. Nevertheless, sumoylation completely blocked the interaction of either form of p53 with SUV39H1 (Fig. 4G). Finally, in SUMO1 knockout mouse retina (Fig. S10), an obvious increase in p53-heterochromatin complex formation was observed (Fig. 4H). These data clearly demonstrate that desumoylation of p53 enhanced its interaction with heterochromatin.

We next sought to determine whether p53 desumoylation is involved in heterochromatin-mediated gene silencing. We first analyzed the relative enrichment of H3K9me3 at p53 target gene promoters in response to p53 WT or K386R overexpression. Compared with WT, K386R overexpression significantly increased H3K9me3 occupancy on p53-regulated proapoptotic target promoters, but not on promoters of antioxidant or cell cycle genes (Fig. 4 I, a). This promoter selection of H3K9me3 coincides well with its specific recruitment to p53-regulated proapoptotic genes on OS exposure (Fig. 3F), which led us to hypothesize that sumoylation may regulate p53 promoter selection. Interestingly, qChIP assay demonstrated similar binding activities of p53 WT and K386R toward proapoptotic gene promoters; however, K386R occupancy was significantly lower than that of Wt on promoters of antioxidant or cell cycle gene (Fig. 4 I, b). Therefore, although desumoylation of p53 enhanced its interaction with heterochromatin, due to decreased binding toward antioxidant genes, the associated heterochromatin was directed to p53-regulated proapoptotic, but not antioxidant, targets.

Finally, we determined the effect of desumoylation of p53 on its transcriptional activity. We found that p53K386R showed significantly lower transcriptional activity on proapoptotic genes in both HCT116 p53$^{+/+}$ and HCT116 p53$^{-/-}$ cells compared with p53 WT (Fig. 4J). Moreover, disruption of heterochromatin completely reversed such reduction observed on p53 K386R (Fig. 4K). Consistently, antioxidant gene expression was not affected by desumoylation of p53 or heterochromatin disruption (Fig. 4K).

Taken together, these results strongly suggest that OS-induced p53 desumoylation plays a critical role in heterochromatin-mediated p53 proapoptotic gene silencing.

Discussion

In the present study, we have obtained the following critical results: (i) OS-induced heterochromatin formation protects RPE cells from apoptosis both in vivo and in vitro; (ii) OS-induced heterochromatin formation is p53-dependent but MDM2-independent; (iii) desumoylation of p53 is critically important for p53 promoter selection and thus for the specific formation of heterochromatins on p53 proapoptotic target gene promoters; and (iv) OS-induced interactions between p53 and heterochromatins at its proapoptotic target gene promoters ensure the suppression of these genes. Together, our results elucidate a critical RPE cell survival function derived from heterochromatin formation and suppression of the p53-dependent apoptotic pathway, which is regulated by p53 desumoylation (Fig. 4K, and Fig. S11).

Previous studies have shown that cumulative OS-induced RPE apoptosis is the major cause of the development of AMD, the primary cause of blindness in elderly (2, 3). It is well known that OS-induced gene expression in RPE cells contributes significantly to RPE apoptosis (2, 3). When facing the OS challenge, RPE cells have different internal mechanisms to defend themselves, with the antioxidative enzymes acting as the first line of defense (26). Our elucidation that heterochromatin senses OS and is selectively formed on p53-regulated proapoptotic gene promoters represents an important protection mechanism. We note that induction of heterochromatin cannot fully protect RPE from OS-triggered degeneration, suggesting the existence of other cell death pathways irrelative to p53-regulated apoptosis. In fact, p53 itself can mediate nonapoptotic cell death, such as necroptosis (27) and pyroptosis (28). Further studies are needed to investigate whether heterochromatin has any effect on these pathways.

Here we have demonstrated that heterochromatin disorganization causes pathological death of RPE cells in vitro and in the AMD mouse model, which likely contributes to development of AMD. Our ongoing studies will try to demonstrate the direct involvement of heterochromatin disruption in AMD pathogenesis in patient. Our results are consistent with recent studies showing that disruption of heterochromatin is critically involved in several human diseases (8, 9, 29, 30), and is thought to be a driving force in premature senescence and breast cancer (8, 30). Depending on the cell type and physiological context, OS-induced heterochromatin dynamics occurs in different ways. Increased heterochromatin formation was detected in mouse embryonic fibroblasts, whereas decreased H3K9me3 was found in Drosophila neurons. Nevertheless, the protective roles of heterochromatin were observed in both studies (29, 31).

Here we also reveal a hitherto unrecognized cytotoxic effect of the heterochromatin noncoding satellite RNAs. Interestingly, a group of short interspersed repetitive RNA, Alu, was recently found to be accumulated in the RPE of AMD patients and in RPE cells on OS exposure, inducing RPE cytotoxicity and degeneration (32, 33). We also detected elevated Alu RNA accumulation after OS exposure, but the expression was regulated differentially from satellite transcription, as was previously found in tumor suppressor depletion-induced heterochromatin disruption (8). Based on the decreased RPE cell viability on satellite overexpression, aberrant satellite expression may present a pathogenic process that contributes to RPE degeneration and AMD in vivo.

Our findings show that heterochromatin protects cells by transcriptionally suppressing the p53 apoptotic signaling pathway. In cancer cells, p53-DNA binding was prevented by adenoviral protein-mediated heterochromatin assembly on p53 target promoters (24). However, we found OS-induced heterochromatin did not exclude p53 from its target promoters; instead, p53 was required for heterochromatin-mediated p53

Gong et al.

CELL BIOLOGY

www.manaraa.com

target gene silencing. We also found OS-induced interactions between p53 and SUV39H1. It was previously reported that p53-SUV39H1 complex formation is mediated by MDM2 (25). Chemotherapy drugs that increased p53 protein led to MDM2-regulated SUV39H1 degradation and, thus to abrogation of the H3K9me3 mark on p53 target promoters (11). Our present findings indicate that the OS-induced p53–heterochromatin interaction was independent of MDM2 based on three lines of evidence: (*i*) in the presence of OS, p53 protein levels were unaltered and thus unlikely to activate the MDM2 negative-feedback loop; (*ii*) p53 was hyperphosphorylated and dissociated from MDM2 under OS; (*iii*) increased rather than reduced H3K9me3 was found on the p53 target promoters on OS, disproving the "eraser" activity of MDM2 on the heterochromatin mark.

p53 is known to activate both proapoptotic and antioxidant genes, depending on the threshold of OS (34). Although p53-regulated cell fate decision between growth arrest and apoptosis have been well studied (35–37), little is known about the mechanism mediating p53 selection on proapoptotic vs. antioxidant target genes. Here we show for the first time that OS-induced desumoylation of p53 regulates p53 promoter selection, enhances its interaction with heterochromatin, and thus preferentially represses proapoptotic genes and protects RPE cells from oxidative damage. Reconstituted SUMO1-p53 protein has been reported to abolish the DNA-binding activity of p53 in vitro (13). However, by using the K386R desumoylation mutant, our study showed that sumoylation enhances p53 binding to proapoptotic genes and activates their transcription in both RPE and HCT116 cells, while the antioxidant genes are irresponsive to p53 sumoylation. This controversial observation may be derived from in vitro and in vivo conditions, as well as the internal promoter selection under p53 sumoylation. Of course, further genome-wide comparison of the DNA-binding and transcriptional activity of p53 WT and K386R is needed to obtain comprehensive information.

Finally, we propose that targeting heterochromatin provides a potential strategy for AMD treatment. Here we found that resveratrol, a well-recognized antioxidant compound, protects RPE cells from OS, significantly increased heterochromatin formation in a dose-dependent manner. We are currently in the process of testing other heterochromatin-promoting drugs with regard to RPE cell protection under OS.

Methods

Animals. The SUMO1 knockout mouse model was generated by coinjection of Cas9 mRNA and short guide RNA (sgRNA) (Fig. S10), as described previously (29). In brief, superovulated female 129 Svj mice were mated to male 129 Svj mice, and embryos were collected from oviducts. Cas9 mRNA (100 ng/μL), two sgRNAs targeting the SUMO1 loci (50 ng/μL) were coinjected into the pronuclei of one-cell embryos. The injected embryos were then transplanted into pseudopregnant mice. At 1 wk after birth, genomic DNA from the toes or tail of the newborn F0 mice was extracted for sequencing. Mice were housed in standard cages in a specific pathogen-free facility on a 12-h light/dark cycle with ad libitum access to food and water. All experimental procedures involving animals were approved by the Animal Use and Care Committee of Zhongshan Ophthalmic Center at Sun Yat-sen University, Guangzhou, China.

NaIO$_3$ Injection. Four-week-old C57BL/6J mice were used in this experiment. A sterile 1% NaIO$_3$ solution was freshly prepared from solid NaIO$_3$ (193979; MP Biomedicals), diluted in PBS. Mice were anesthetized with isoflurane/oxygen and injected with 70 mg/kg NaIO$_3$ via the orbital venous plexus as described previously (30, 31). Control mice were injected with similar volumes of PBS. For chaetocin treatment, mice were treated six times per wk by oral gavage with polyethylene glycol 400 (PEG400) or 0.25 mg/kg chaetocin (in 0.17% DMSO, 20% PEG400 and the remainder PBS) for 1 wk before i.p. injection of NaIO$_3$.

RPE Extraction. Two posterior eye cups (sclera-choroid-RPE cups) from the same mouse were combined and subjected to RNA extraction. Total RNA

from RPE cells was isolated using the simultaneous RPE cell isolation and RNA stabilization (SRIRS) method (32). In brief, the RPE cells were isolated using RNAprotect cell reagent (76526; QIAGEN). Total RNA extraction was performed using the RNAprep Pure Kit (DP430; Tiangen) with ~100–200 ng RNA obtained from two eye cups.

MNase Digestion Assay. The procedure has been described in detail previously (33). In brief, 2.5×10^5 hRPE cells were used for one digestion. The genomic DNA was extracted by phenol/chloroform (pH 8), and 2–4 U MNase was used to digest the DNA at room temperature for 5 min. The digested DNA was examined by 1.2% agarose electrophoresis.

Histology and IF. For immunohistochemistry analysis of the posterior eye cups, the neural retina was dissected out, and the RPE/choroid eye cup was fixed in 4% paraformaldehyde for 30 min. RPE cell-containing eye cups were then flattened by making long radial cuts, followed by incubation in a blocking buffer containing 5% BSA and 0.02% Triton X-100 for 2 h at room temperature. RPE flat mounts were incubated with anti-H3K9me3 (8898, 1:100; Abcam) primary antibodies overnight at 4 °C, followed by a 2-h incubation with the secondary antibody (A11034, 1:200; Invitrogen). F-actin was labeled by FITC phalloidin (40735ES75; Yeasen Biotechnology). The procedure for IF in human RPE cells has been described previously (10). The images were captured with a Zeiss LSM 800 confocal microscope.

Cell Culture and Reagents. ARPE-19 cells were purchased from American Type Culture Collection. hRPE cells from 25-wk-old embryos were kindly provided by H.O. ARPE-19 and hRPE cells were maintained in DMEM supplemented with 10% FBS. For hRPE cell culture, 15 μg/mL Laminin (L2020; Sigma-Aldrich) was used to coat the plate. Lipofectamine 3000 transfection reagent was purchased from Life Technologies.

Drug Treatment. The generation of OS by GO treatment (1673; MP Biomedicals) has been described previously (34). To stably supply RPE cells with H$_2$O$_2$, confluent cells were cultured in a final concentration of 10 mU/mL GO in the serum-free medium. Chaetocin (C9492; Sigma-Aldrich), resveratrol (S1396; Selleck), and IL-18 (Sino Biological) were added to cells cultured in serum-free medium for 24 h with or without further GO treatment.

RT-PCR and qPCR. RT-PCR and qPCR were conducted as described previously (10). Total RNA was extracted using the RNAprep Pure Kit (DP430; Tiangen), in which the genomic DNA was removed by DNase I digestion. cDNA synthesis was performed with 1 μg of total RNA using the RevertAid First-Strand cDNA Synthesis Kit (K1622; Thermo Fisher Scientific). Gene expression levels were analyzed using SuperReal PreMix Plus (SYBR Green) (FP205; Tiangen) and the LightCycler 480 qPCR system (Roche). The assays were performed in triplicate, and the Ct values were normalized to 18S rRNA or GAPDH. The primers used are listed in Table S1.

Cell Viability Assay. Cell viability was determined by the MTT assay as described previously (34)

ChIP and ChIP-Seq. ChIP assays were conducted as described previously (35). In brief, 20–30 μg of chromatin obtained from ARPE-19 or hRPE cells was used for each IP. The corresponding proteins were precipitated using 10 μg of p53 antibody (sc-126; Santa Cruz Biotechnology), 5 μg of H3K9me3 antibody (8898; Abcam), or 5 μg of FLAG antibody (F1804; Sigma-Aldrich), with 2 μg of normal rabbit IgG (sc-2027; Santa Cruz) or mouse IgG (sc-2343; Santa Cruz Biotechnology) as a negative control. The antibodies or IgGs were incubated with the chromatin overnight at 4 °C. The precipitated chromatin was purified using the QIAquick PCR Purification Kit (28104; QIAGEN) and analyzed by qPCR using the primers listed in Table S1. The readouts were normalized using 2% input chromatin for each sample.

For the ChIP-seq analyses, the precipitated DNA and inputs were sent to CapitalBio Technology for sequencing. In brief, the libraries were prepared from 10 ng of each ChIP and input sample using the NEBNext Ultra DNA Library Prep Kit for Illumina (E7370S/L; New England BioLabs). Libraries were clonally amplified in a flow cell and sequenced with the Illumina HiSeq X 10 System to generate paired-end sequences. ARPE-19 cells from two independent experiments were used for the ChIP-seq, and the sum of sequenced reads from two samples was subjected to following analyses. Sequenced reads were mapped to the human genome (hg19) with bowtie1 (mismatch = 2) (38). Paired reads uniquely mapped to the genome were extracted using samtools version 0.1.18 (SourceForge). The peaks were called using a model-based analysis of ChIP-seq (macs14) (39), with $P < 10^{-5}$ as a

threshold. Peaks were annotated with ChIPseeker (40). Raw data have been submitted to the National Center for Biotechnology Information's Sequence Read Archive database (https://www.ncbi.nlm.nih.gov/sra) under accession no. SRP132687.

Immunoprecipitation. IP was performed as described previously (10). hRPE cells were used for the co-IP assays. Whole-cell extracts were prepared with lysis buffer (25 mM Tris·HCl pH 7.4, 150 mM NaCl, 5% glycerol, 1% Nonidet P-40, and 1 mM EDTA) and precleared with Protein A/G PLUS-agarose beads (sc-2003; Santa Cruz Biotechnology) and 1 μg of mouse IgG. The cellular extracts were incubated with anti-p53 antibody (sc-126; Santa Cruz Biotechnology) or anti-FLAG antibody (F1804; Sigma-Aldrich) overnight and then incubated with Protein A/G PLUS-agarose beads for 4 h at 4 °C. The immunocomplex was eluted in loading buffer by boiling at 95 °C for 5 min and then subjected to WB analysis. For detection of sumoylated p53, freshly prepared 20 mM NEM was added during cell lysis and washing steps.

Apoptosis Assay. Cell apoptosis determined by flow cytometry was performed with the PE Annexin V Apoptosis Detection Kit I (559763; BD Pharmingen). The stained cells were analyzed with a BD LSRFortessa Cell analyzer (649225; BD Biosciences). TUNEL assays were performed using the Roche In Situ Cell Death Detection Kit (11684817910) in accordance with the manufacturer's instructions.

Plasmids and siRNA. The mouse GFP-Maj Sat and human GFP-Satα were kindly provided by Inder Verma (8). FLAG-SUV39H1 and HA-SUV39H1 plasmids were purchased from Sino Biological and verified by sequencing.

Microarray Analysis. ARPE-19 cells of 90% confluence were transfected with GFP or GFP-Sat α. After 48 h, cells were lysed/stored in TRIzol reagent before being sent for microarray analysis by Shanghai Biotechnology. In brief, RNA was extracted using the RNeasy Mini Kit (P/N74104; QIAGEN). Total RNAs were amplified, biotin-labeled, and purified using the GeneChip 3' IVT PLUS Reagent Kit (902416; Affymetrix). cRNA was then hybridized to the GeneChip PrimeView Human Gene Expression Array (Affymetrix). Slides were scanned with a GeneChip Scanner 3000 (Affymetrix) using Command Con-sole Software 4.0 (Affymetrix) with default settings. Raw data were normalized by the MAS 5.0 and RMA algorithm Affymetrix packages in R. A heatmap was generated from the normalized microarray data using Cluster 3.0. Pathway enrichment analysis was performed using DAVID Bioinformatics Resources version 6.7. Raw data have been submitted to the Gene Expression Omnibus database (https://www.ncbi.nlm.nih.gov/geo/) under accession no. GSE100691.

In Vitro Sumoylation Assay. The in vitro sumoylation assay was conducted using a sumoylation kit (#BML-UW8955-001; Enzo Life Science) as described previously (36). Briefly, 2.5 μg of purified FLAG-p53 WT or FLAG-p53K386R proteins was used for each 20-μL reaction systems.

In Vitro Protein Interaction. HA-SUV39H1 plasmid was transfected into HCT-116 p53$^{-/-}$ cells. After 72 h, cells were lysed in RIPA buffer, and 10 μg of HA antibody (3724; Cell Signaling Technology) or 5 μg of rabbit IgG was added to immunoprecipitate the HA-SUV39H1 protein. The protein-bead complexes were washed three times with RIPA buffer and then three times with binding buffer (50 mM Tris·HCL, pH 7.5). p53 proteins (sumoylated or unsumoylated) were incubated with SUV39H1 or IgG beads overnight at 4 °C with gentle shaking. After incubation, the beads were washed three times with binding buffer, and the interacting complex was then resolved by boiling in Laemmli buffer for 5 min.

Statistics. Significance was calculated using the unpaired t test. Differences were considered statistically significant at $P < 0.05$. All values are presented as mean ± SD of the number of determinations.

1. Fuhrmann S, Zou C, Levine EM (2014) Retinal pigment epithelium development, plasticity, and tissue homeostasis. *Exp Eye Res* 123:141–150.
2. Cai J, Nelson KC, Wu M, Sternberg P, Jr, Jones DP (2000) Oxidative damage and protection of the RPE. *Prog Retin Eye Res* 19:205–221.
3. Plafker SM, O'Mealey GB, Szweda LI (2012) Mechanisms for countering oxidative stress and damage in retinal pigment epithelium. *Int Rev Cell Mol Biol* 298:135–177.
4. Wang J, Jia ST, Jia S (2016) New insights into the regulation of heterochromatin. *Trends Genet* 32:284–294.
5. Grewal SI, Jia S (2007) Heterochromatin revisited. *Nat Rev Genet* 8:35–46.
6. Rea S, et al. (2000) Regulation of chromatin structure by site-specific histone H3 methyltransferases. *Nature* 406:593–599.
7. Guenatri M, Bailly D, Maison C, Almouzni G (2004) Mouse centric and pericentric satellite repeats form distinct functional heterochromatin. *J Cell Biol* 166:493–505.
8. Zhu Q, et al. (2011) BRCA1 tumour suppression occurs via heterochromatin-mediated silencing. *Nature* 477:179–184.
9. Ting DT, et al. (2011) Aberrant overexpression of satellite repeats in pancreatic and other epithelial cancers. *Science* 331:593–596.
10. Gong L, et al. (2015) Nuclear PTEN tumor-suppressor functions through maintaining heterochromatin structure. *Cell Cycle* 14:2323–2332.
11. Mungamuri SK, et al. (2012) p53-mediated heterochromatin reorganization regulates its cell fate decisions. *Nat Struct Mol Biol* 19:478–484.
12. Mungamuri SK, et al. (2016) USP7 enforces heterochromatinization of p53 target promoters by protecting SUV39H1 from MDM2-mediated degradation. *Cell Rep* 14:2528–2537.
13. Wu SY, Chiang CM (2009) Crosstalk between sumoylation and acetylation regulates p53-dependent chromatin transcription and DNA binding. *EMBO J* 28:1246–1259.
14. Rodriguez MS, et al. (1999) SUMO-1 modification activates the transcriptional response of p53. *EMBO J* 18:6455–6461.
15. Gostissa M, et al. (1999) Activation of p53 by conjugation to the ubiquitin-like protein SUMO-1. *EMBO J* 18:6462–6471.
16. Enzmann V, et al. (2006) Behavioral and anatomical abnormalities in a sodium iodate-induced model of retinal pigment epithelium degeneration. *Exp Eye Res* 82:441–448.
17. Kaczara P, Sarna T, Burke JM (2010) Dynamics of H_2O_2 availability to ARPE-19 cultures in models of oxidative stress. *Free Radic Biol Med* 48:1064–1070.
18. Ziv Y, et al. (2006) Chromatin relaxation in response to DNA double-strand breaks is modulated by a novel ATM- and KAP-1–dependent pathway. *Nat Cell Biol* 8:870–876.
19. Ijima R, et al. (2014) Interleukin-18 induces retinal pigment epithelium degeneration in mice. *Invest Ophthalmol Vis Sci* 55:6673–6678.
20. Greiner D, Bonaldi T, Eskeland R, Roemer E, Imhof A (2005) Identification of a specific inhibitor of the histone methyltransferase SU(VAR)3-9. *Nat Chem Biol* 1:143–145.
21. Lagouge M, et al. (2006) Resveratrol improves mitochondrial function and protects against metabolic disease by activating SIRT1 and PGC-1alpha. *Cell* 127:1109–1122.
22. Sheu SJ, et al. (2013) Resveratrol stimulates mitochondrial bioenergetics to protect retinal pigment epithelial cells from oxidative damage. *Invest Ophthalmol Vis Sci* 54:6426–6438.
23. Lachner M, O'Carroll D, Rea S, Mechtler K, Jenuwein T (2001) Methylation of histone H3 lysine 9 creates a binding site for HP1 proteins. *Nature* 410:116–120.
24. Soria C, Estermann FE, Espantman KC, O'Shea CC (2010) Heterochromatin silencing of p53 target genes by a small viral protein. *Nature* 466:1076–1081.
25. Chen L, et al. (2010) MDM2 recruitment of lysine methyltransferases regulates p53 transcriptional output. *EMBO J* 29:2538–2552.
26. Imamura Y, et al. (2006) Drusen, choroidal neovascularization, and retinal pigment epithelium dysfunction in SOD1-deficient mice: A model of age-related macular degeneration. *Proc Natl Acad Sci USA* 103:11282–11287.
27. Montero J, Dutta C, van Bodegom D, Weinstock D, Letai A (2013) p53 regulates a non-apoptotic death induced by ROS. *Cell Death Differ* 20:1465–1474.
28. Gupta S, Radha V, Furukawa Y, Swarup G (2001) Direct transcriptional activation of human caspase-1 by tumor suppressor p53. *J Biol Chem* 276:10585–10588.
29. Frost B, Hemberg M, Lewis J, Feany MB (2014) Tau promotes neurodegeneration through global chromatin relaxation. *Nat Neurosci* 17:357–366.
30. Zhang W, et al. (2015) Aging stem cells: A Werner syndrome stem cell model unveils heterochromatin alterations as a driver of human aging. *Science* 348:1160–1163.
31. Bosch-Presegué L, et al. (2011) Stabilization of Suv39H1 by SirT1 is part of oxidative stress response and ensures genome protection. *Mol Cell* 42:210–223.
32. Kaneko H, et al. (2011) DICER1 deficit induces Alu RNA toxicity in age-related macular degeneration. *Nature* 471:325–330.
33. Tarallo V, et al. (2012) DICER1 loss and Alu RNA induce age-related macular degeneration via the NLRP3 inflammasome and MyD88. *Cell* 149:847–859.
34. Sablina AA, et al. (2005) The antioxidant function of the p53 tumor suppressor. *Nat Med* 11:1306–1313.
35. Sen N, Kumari R, Singh MI, Das S (2013) HDAC5, a key component in temporal regulation of p53-mediated transactivation in response to genotoxic stress. *Mol Cell* 52:406–420.
36. Le Cam L, et al. (2006) E4F1 is an atypical ubiquitin ligase that modulates p53 effector functions independently of degradation. *Cell* 127:775–788.
37. Mayo LD, et al. (2005) Phosphorylation of human p53 at serine 46 determines promoter selection and whether apoptosis is attenuated or amplified. *J Biol Chem* 280:25953–25959.
38. Langmead B, Trapnell C, Pop M, Salzberg SL (2009) Ultrafast and memory-efficient alignment of short DNA sequences to the human genome. *Genome Biol* 10:R25.
39. Zhang Y, et al. (2008) Model-based analysis of ChIP-seq (MACS). *Genome Biol* 9:R137.
40. Yu G, Wang LG, He QY (2015) ChIPseeker: An R/Bioconductor package for ChIP peak annotation, comparison and visualization. *Bioinformatics* 31:2382–2383.

CELL BIOLOGY

Gong et al.

www.manaraa.com